




Tunable metal contacts at layered black-arsenic/ metal interface forming during metal deposition for device fabrication

Subhajit Kundu¹, Prafful Golani², Hwanhui Yun ¹, Silu Guo¹, Khaled M. Youssef ³, Steven J. Koester ² & K. Andre Mkhoyan ¹✉

Understanding the kinetics of interfacial reaction in the deposition of metal contacts on 2D materials is important for determining the level of contact tenability and the nature of the contact itself. Here, we find that some metals, when deposited onto layered black-arsenic films using e-beam evaporation, form a few-nm thick distinct intermetallic layer and significantly change the nature of the metal contact. In the case of nickel, the intermetallic layer is Ni₁₁As₈, whereas in the cases of chromium and titanium they are CrAs and α-Ti₃As, respectively, with their unique structural and electronic properties. We also find that temperature, which affects interatomic diffusion and interfacial reaction kinetics, can be used to control the thickness and crystallinity of the interfacial layer. In the field effect transistors with black-arsenic channel, due to the specifics of its formation, this interfacial layer introduces a second and more efficient edge-type charge transfer pathway from the metal into the black-arsenic. Such tunable interfacial metal contacts could provide new pathways for engineering highly efficient devices and device architectures.

¹Department of Chemical Engineering and Materials Science, University of Minnesota, 421 Washington Ave. SE, Minneapolis, MN 55455, USA.

²Department of Electrical and Computer Engineering, University of Minnesota, 200 Union St. SE, Minneapolis, MN 55455, USA. ³Materials Science and Technology Graduate Program, College of Arts and Sciences, Qatar University, 100 Aljamaa St., Doha 2713, Qatar. ✉email: mkhoyan@umn.edu

Many two-dimensional (2D) layered nanocrystals like graphene, transition-metal dichalcogenides (TMDs), black phosphorous (b-P), and others have been predicted and experimentally proven to have properties that are significantly different or enhanced than their bulk counterparts^{1–8}. Superconducting, metallic, semiconducting, and topological properties of these materials with a possibility to be only a-few-atom-thick makes them desirable components for next-generation optoelectronic devices, field-effect transistors (FETs), valley electronics, and spintronics^{9–13}. Recently, black-arsenic (b-As), an allotrope of As with a structure similar to b-P, has shown remarkable in-plane anisotropy in thermal and electrical transport properties along with mechanical and vibrational anisotropy^{14,15}. Even at its early stage, b-As has shown considerable promise for advanced optoelectronic device applications^{16,17}. The functionality and efficiency of b-As in devices, as for other 2D layered materials, largely rely on charge injection into or from it via the metallic contacts^{18–24}. Recent atomic-resolution electron microscopy study of the metal-MoS₂ contacts²⁵ has shown that for some metals the inherent chemistry between them and the layered material could lead to unexpected formations—nanovoids, degraded layers, and interfused regions—highlighting the importance of understanding the metal contacts with b-As at the atomic-scale.

For b-As/metal and for other 2D-materials/metal contacts the kinetics of interfacial reactions determines the level of contact tenability, which can be adjusted by changing the metal deposition conditions such as deposition temperature, rate, substrate temperature etc²⁶. Therefore, for the applicability of this newly discovered 2D b-As in the devices, understanding the kinetics of these metal/b-As interfacial reactions becomes as important as the understanding of the nature of the contact itself.

Here, we report analytical scanning transmission electron microscopy (STEM) study of the metal/b-As contact, where several e-beam evaporated metals were considered. We discovered that, in the case of Ni, under typical metal deposition conditions metal/b-As contact is not a conventional contact but a layer of polycrystalline intermetallic Ni₁₁As₈ with its own unique structural and electronic properties. Additionally, a series of in situ heating experiments showed that this phenomenon is not unique for Ni but can be present with other metal contacts. By adjusting the parameters of interfacial reaction kinetics intermetallic layers of various thicknesses can be formed at the Cr/b-As and Ti/b-As interface as well.

Results and discussion

The metal contact formed at b-As/Ni interface was studied using analytical STEM after transferring thin-film b-As onto Si/SiO₂ substrate and depositing metal Ni on top of the b-As film by e-beam evaporation (see Methods section). This procedure for making b-As/metal contact is identical to the one used for making b-As-based devices allowing direct comparison of the characteristics of b-As/Ni contact with the device performance. For all STEM samples, layers of amorphous carbon and platinum were deposited on the top of deposited Ni for protection and then the stack was cross-sectionally cut into lamellae using a focus ion beam (FIB) (Fig. 1a–c).

When the lamellae of the stack were examined in STEM, it was apparent that dramatic changes have occurred at the b-As/Ni interface. About 13-nm-thick (13.3 ± 3.7 nm, when evaluated across many samples) brighter layer inside b-As, adjacent to Ni contact, can be readily identified in composition-sensitive annular dark-field (ADF)-STEM images (Fig. 1c). Small voids at the interface between this layer and Ni are also visible. Outside this new layer, the b-As film appears to be completely unaffected and van der Waals (vdW) bonded atomic layers of b-As running

parallel to the substrate can be readily visualized in high-resolution ADF-STEM images²⁷. In conventional bright-field (BF) transmission electron microscopy (TEM) images this new layer has the characteristics of a polycrystalline film. Strong diffraction contrast present in this layer, that changes from one grain to another, is similar to that in the evaporated polycrystalline Ni layer (Fig. 1d). The compositional analysis carried out in STEM using energy-dispersive x-ray (EDX) spectroscopy-based elemental mapping shows that this polycrystalline layer is about 60–40 at.% mixture of Ni and As (Fig. 1e, f). While the layer being As-Ni mixture (NiAs_x) explains the brighter contrast in Z-sensitive ADF-STEM images, determination of the phase of this alloy and the origin of its formation required additional analysis.

To evaluate the phase of the NiAs_x interface layer and to understand the origin of its formation, two different sets of in situ TEM heating experiments were conducted. In the first set, the sample was gradually heated from room temperature ($T_R = 22^\circ\text{C}$) to $T = 292^\circ\text{C}$ at a rate of $19^\circ\text{C}/\text{min}$. As the temperature of the entire lamellae gradually increases, it was observed that the interfacial polycrystalline NiAs_x layer expands and the grains inside the layer become larger. This transformation is visualized in a series of conventional TEM images (Fig. 2a). The diffraction patterns obtained from the structure along with BF-TEM images further support the observations. As can be seen from these images the expansion of the interfacial NiAs_x layer is supported by the diffusion of Ni from the top layer. Hence, an increase in temperature promotes: (i) Ni diffusion from the top pure Ni layer into b-As resulting in the formation of a new crystalline NiAs_x phase and (ii) grain growth inside this new phase. After reaching $T = 292^\circ\text{C}$ and seeing almost complete absorption of Ni into b-As and formation of large-grain (100–300 nm) crystalline NiAs_x, the samples were cooled down to T_R for phase identification using atomic-resolution ADF-STEM imaging and STEM-EDX compositional analysis. High-resolution ADF-STEM images obtained from two different crystallographic orientations (along [031] and [100] directions) identify the phase as the intermetallic compound Ni₁₁As₈. ADF-STEM image simulations for Ni₁₁As₈ further confirmed the observations.

Atomic-resolution ADF-STEM images presented in Fig. 2b, c show the tetragonal crystal structure of Ni₁₁As₈ (also known as Maucherite and has lattice parameters: $a = b = 6.872 \text{ \AA}$, and $c = 21.821 \text{ \AA}$) with the distinct atomic arrangement when viewed along [100] crystallographic direction²⁸. The STEM-EDX compositional analysis of (60 at.%-Ni)/(40 at.%-As) mixture obtained before and after heating experiments (Figs. 1e, f, 2d) and appearance of new spots in diffraction patterns corresponding to reflections from (211) plane of Ni₁₁As₈ (Fig. 2a and Supplementary Fig. 1) further support this phase identification. The formation of the Ni₁₁As₈ phase is also energetically favorable among known NiAs compounds due to its highest negative formation energy ($\Delta G_0 = -0.308 \text{ eV}$) and lowest melting point ($T_m = 830^\circ\text{C}$)^{29,30}. It should be noted that in diffusion couple experiments similar to the one studied here, even though small amounts of other phases can form during the course of annealing, the grains having the phase with the lowest melting point grow in size, whereas the other phases die out³¹. Small grains of the Ni₁₁As₈ phase were readily detected in atomic-resolution ADF-STEM images of the initial polycrystalline interfacial layer (see Supplementary Fig. 2). The dependence of grain size in this interfacial Ni₁₁As₈ layer on temperature was also evaluated (see Supplementary Fig. 3).

In the second set of in situ experiments, the temperature of the lamellae of the layer stack was increased quickly in about 12 min to reach a temperature $>200^\circ\text{C}$ and kept at the constant temperature. For these experiments, two different final temperatures

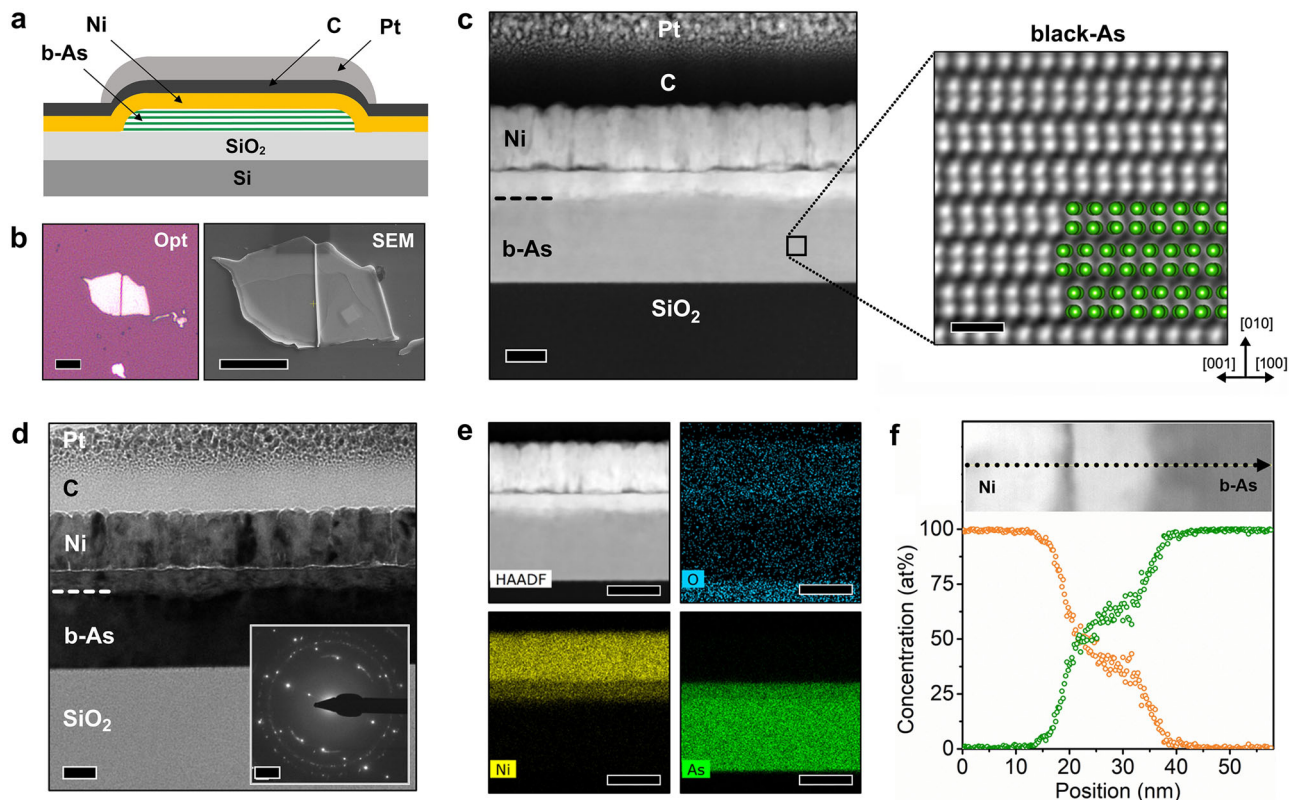


Fig. 1 Observation of NiAs_x interfacial layer formation during nickel contact deposition. **a** Schematic of the sample in cross-section showing all the layers present in the stack. **b** Optical image of a b-As thin flake after transferring it onto Si/SiO₂ substrate (left) and scanning electron microscope (SEM) image of the same flake after depositing 50 nm Ni, amorphous carbon, and platinum on the top and before FIB cutting a lamella. Scale bars are 10 μm. **c** Low-magnification ADF-STEM image of the stack showing all the layers in the stack. It also shows the presence of a bright layer inside the b-As film close to the b-As/Ni interface. The scale bar is 30 nm. Atomic-resolution image on the right shows vdW bonded atomic layers of b-As facing deposited Ni layer with overlaid model-oriented along [101] zone axis (image was band-pass filtered for clarity). Scale bar is 1 nm. **d** BF-TEM image of the same stack as in (c) showing single-crystal b-As, polycrystalline Ni, and the new layer inside b-As close to the interface. Inset, diffraction pattern from the layer stack when b-As is oriented along [101] zone axis. Scale bars are 30 nm and 1 nm⁻¹. **e** ADF-STEM image and complimentary EDX elemental maps: O (blue), As (green), and Ni (yellow); showing the elemental distributions. Light surface oxidation of the metal layers due to sample preparation is expected and observed. Scale bar is 50 nm. **f** Quantified EDX line scan obtained across the b-As/Ni interface (marked by a dotted arrow on the ADF-STEM image on the top) show about 60 at.% Ni and 40 at.% As in the bright layer inside b-As. The EDX elemental maps are based on As and Ni K signals.

were considered: $T_1 = 267^\circ\text{C}$ and $T_2 = 208^\circ\text{C}$ (for details see Supplementary Fig. 4). The overall outcome of these experiments was similar to those in the first set of experiments; the interfacial Ni₁₁As₈ layer expands with time due to diffusion of Ni from the top deposited Ni layer into the b-As film until (i) all b-As is transformed or (ii) all Ni is consumed, and the grains inside the Ni₁₁As₈ layer increase in size. These changes in the layers were captured in TEM images (Fig. 3a).

For quantification of the transformation of the b-As film into Ni₁₁As₈ due to Ni diffusion, the thickness of the Ni₁₁As₈ layer, d , was plotted versus \sqrt{t} showing linear behavior for both temperatures: $T_1 = 267^\circ\text{C}$ and $T_2 = 208^\circ\text{C}$ (Fig. 3b, c). Using a “thin-film” diffusion model and diffusion length of $d = 4\sqrt{D(T)t}$, with a diffusion coefficient of $D(T) = D_0 \exp\left\{-\frac{Q}{k_B T}\right\}$, from two slopes of d vs \sqrt{t} (13.2 nm min^{-1/2} for T_1 and 1.77 nm min^{-1/2} for T_2), the activation energy and diffusion constant were determined to be $Q = 1.53$ eV and $D_0 = 1.93 \times 10^{15}$ nm² min⁻¹, respectively. With such diffusion coefficient at T_R Ni diffuse into b-As is expected to be extremely ($\times 10^{-5}$ – 10^{-6}) slower. These results also suggest that the Ni layer should have been deposited onto the b-As film at an elevated temperature of about $T_{\text{dep}} = 230^\circ\text{C}$, considering the Ni deposition time was only $t_{\text{dep}} = 10$ min (for details see Supplementary Fig. 5), which is about 180°C higher

than the temperature of the substrate/chamber during the Ni deposition. It has been reported that, when 80–20% Ni-Fe Permalloy thin film was vacuum-evaporated on a glass substrate, film deposition temperature was 128°C higher than that of substrate³². Considering that the melting point of Ni-Fe Permalloy is $T_m^P = 1435^\circ\text{C}$, which is about 20°C lower than the melting point of Ni and differences in deposition rates, these two observations appear to be consistent with each other. Based on the activation energy and diffusion constant determined from these measurements, it is estimated that formation of Ni₁₁As₈ layer can be expected even at considerably lower ($\lesssim 150^\circ\text{C}$) deposition temperatures (Fig. 3d), which puts limitations on Ni contact deposition on b-As as well as on lifetime and performance of such devices at elevated temperatures.

The effect of elevated temperature on device performance was tested on FET built with a b-As channel and a global SiO₂/Si back gate (Fig. 3e). The electrical characteristics of these FETs were reported earlier¹⁷. It should be noted that these devices even at T_R have this new kind of metal contact. The interfacial metallic Ni₁₁As₈ is the layer contacting b-As, and therefore, two different charge transfer paths from Ni₁₁As₈ contact into b-As are in play here, one across the vdW gap between Ni₁₁As₈ and vdW bonded layers of b-As and the second through metallic bonds between Ni₁₁As₈ and the sides of b-As layers known as “edge” contact

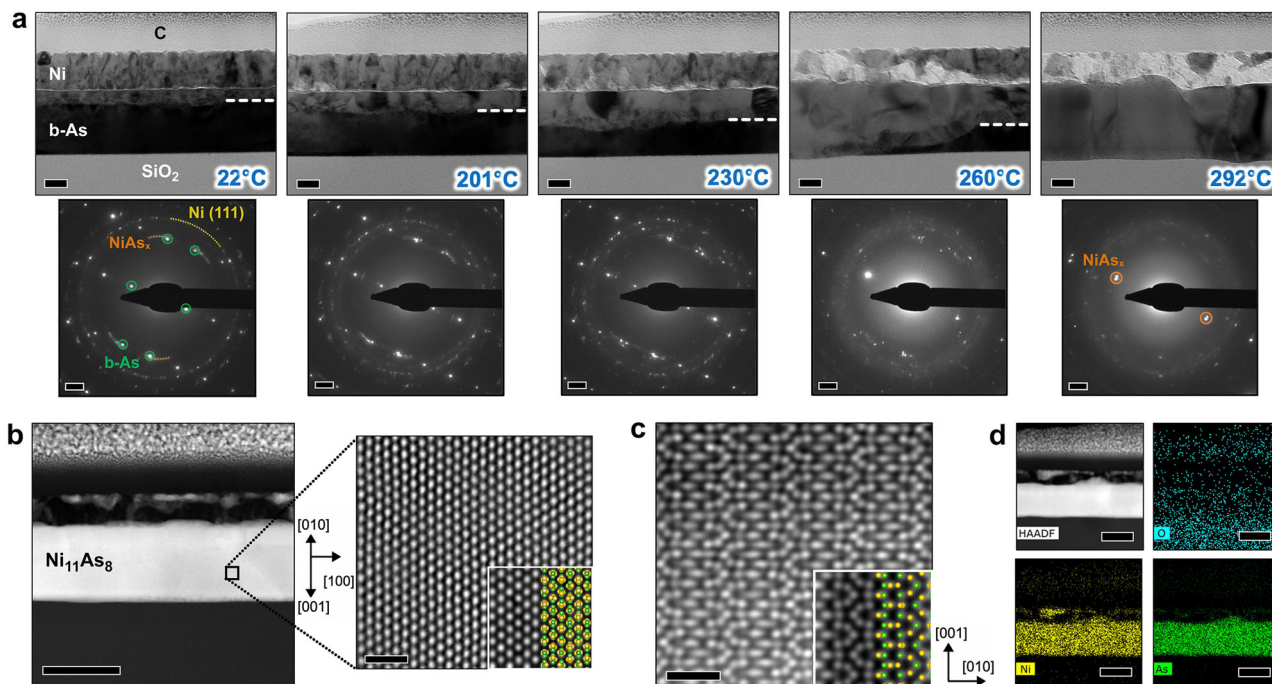


Fig. 2 Changes in NiAs_x interfacial layer during in situ TEM heating. **a** A set of BF-TEM images of the stack of Si/SiO_2 substrate, b-As film, deposited polycrystalline Ni, and the interfacial NiAs_x layer showing a gradual expansion of the NiAs_x layer with an increase of temperature going from $T_R = 22^\circ\text{C}$ to $T = 292^\circ\text{C}$. Grain growth in the NiAs_x layer is also visible. Each image is accompanied by a diffraction pattern (below) obtained from the stack at the same temperature. The layer stack is oriented along $[101]$ zone axis of b-As. Scale bars are 30 nm and 1nm^{-1} . The arced spots in the diffraction pattern at T_R correspond to polycrystalline NiAs_x (marked orange) and Ni layers (marked yellow). Progressive heating leads to the shortening of the arced spots from the polycrystalline NiAs_x layer and the appearance of two strong spots. **b** ADF-STEM images of the stack after reaching $T = 292^\circ\text{C}$ and cooling it down to T_R . A High-resolution ADF-STEM image of the layer shows atomic columns of $\text{Ni}_{11}\text{As}_8$ crystal in $[031]$ zone axis. Scale bars are 100 and 1 nm, respectively. **c** Atomic-resolution ADF-STEM image of the layer from another heating experiment showing the unique pattern of atomic columns of $\text{Ni}_{11}\text{As}_8$ crystal viewed along $[100]$ zone axis. Scale bar is 1 nm. Insets in **(b, c)** are simulated ADF-STEM images of $\text{Ni}_{11}\text{As}_8$ in the same directions. **d** ADF-STEM image of the stack in **(b)** with EDX elemental maps of O (blue), As (green), and Ni (yellow) showing the complete transformation of the b-As film into $\text{Ni}_{11}\text{As}_8$. Light oxidation of the metal layers remains there even after the formation of $\text{Ni}_{11}\text{As}_8$. Scale bar is 100 nm.

(indicated by red arrows in Fig. 3e). The edge contacts between $\text{Ni}_{11}\text{As}_8$ and b-As are expected to be more efficient^{21,33}. According to our earlier observation (Fig. 1), if the thickness of b-As channel is $\lesssim 10\text{nm}$, the contact present should be only edge-type.

When relatively thin b-As channel FET ($d_{\text{b-As}} = 13 \pm 2\text{nm}$, measured by AFM and PFA) was heated to 100°C and then to 150°C and drain current vs gate voltage characteristics were measured, it was observed that at 150°C the FET stops showing characteristic drain current modulation (Fig. 3f). Since at 150°C more Ni is diffused into b-As compared to 100°C , it is likely that the voids at the $\text{Ni}/\text{Ni}_{11}\text{As}_8$ increased to the point that the current path was substantially broken between the Ni to $\text{Ni}_{11}\text{As}_8$, leading to the dramatic reduction in current. The difference between device characteristics at T_R and 100°C is likely due to changes in contact work function caused by grain size increase in $\text{Ni}_{11}\text{As}_8$ and changes in contact structure with temperature increase. SEM analysis of these heated devices shows that, as predicted earlier (Fig. 3d), more Ni diffuses into the b-As and, due to the small thickness of the b-As film, an additional lateral diffusion of Ni occurs transforming the entire channel into $\text{Ni}_{11}\text{As}_8$ (Fig. 3g). Since $\text{Ni}_{11}\text{As}_8$ is metallic, the FET channel stops showing any modulation under the presence of gate bias. However, when b-As channel of the FET is sufficiently thick ($d_{\text{b-As}} \gtrsim 50\text{nm}$), as we observed, mostly areas under the Ni contacts are converted into $\text{Ni}_{11}\text{As}_8$ consuming all deposited Ni (for SEM and STEM analysis see Supplementary Figs. 6, 7), keeping the channel intact.

To examine if such an interfacial contact layer can be formed with other metals, besides Ni, four other metals: Pt, Cr, Ti, and Ge, were also considered. Similar to Ni, these metal layers were deposited on b-As film using the same system and similar procedure, and then FIB-cut into lamellae and studied in STEM. As in the case of Ni, the metal/b-As interfaces were first characterized at T_R , followed by in situ heating inside the microscope, and then characterized again. Selection of these specific metals was based on two factors: (i) their similar or contrasting properties relative to Ni (atomic/ionic radius, valency, electronegativity, melting point, etc.) and (ii) the possibility to deposit them on b-As using the same evaporation system as Ni and same deposition rate (1Å s^{-1}). Among these four metals, two Cr and Ti, showed similar Ni interfacial contact layer formation.

Cr is another transition element similar to Ni, which also forms compounds with As. ADF-STEM imaging and EDX analysis carried out at T_R right after deposition shows that evaporated Cr, which forms a polycrystalline thin film, only lightly diffuses into b-As (Fig. 4a) during deposition. Atomic-resolution images of the interface between b-As and Cr show depletion of Cr at the interface resulting in small voids and formation of about 2–3 layers (or about 1 nm) CrAs_x layer inside b-As (Fig. 4a). However, during in situ heating, Cr shows visible diffusion into the b-As starting at a temperature of 254°C (see Supplementary Fig. 8). Further increase of the temperature to 328°C expedites Cr diffusion and increases the thickness of the interfacial CrAs_x compound layer (Fig. 4a), which is similar to the observations discussed earlier for deposited Ni but at higher temperatures and

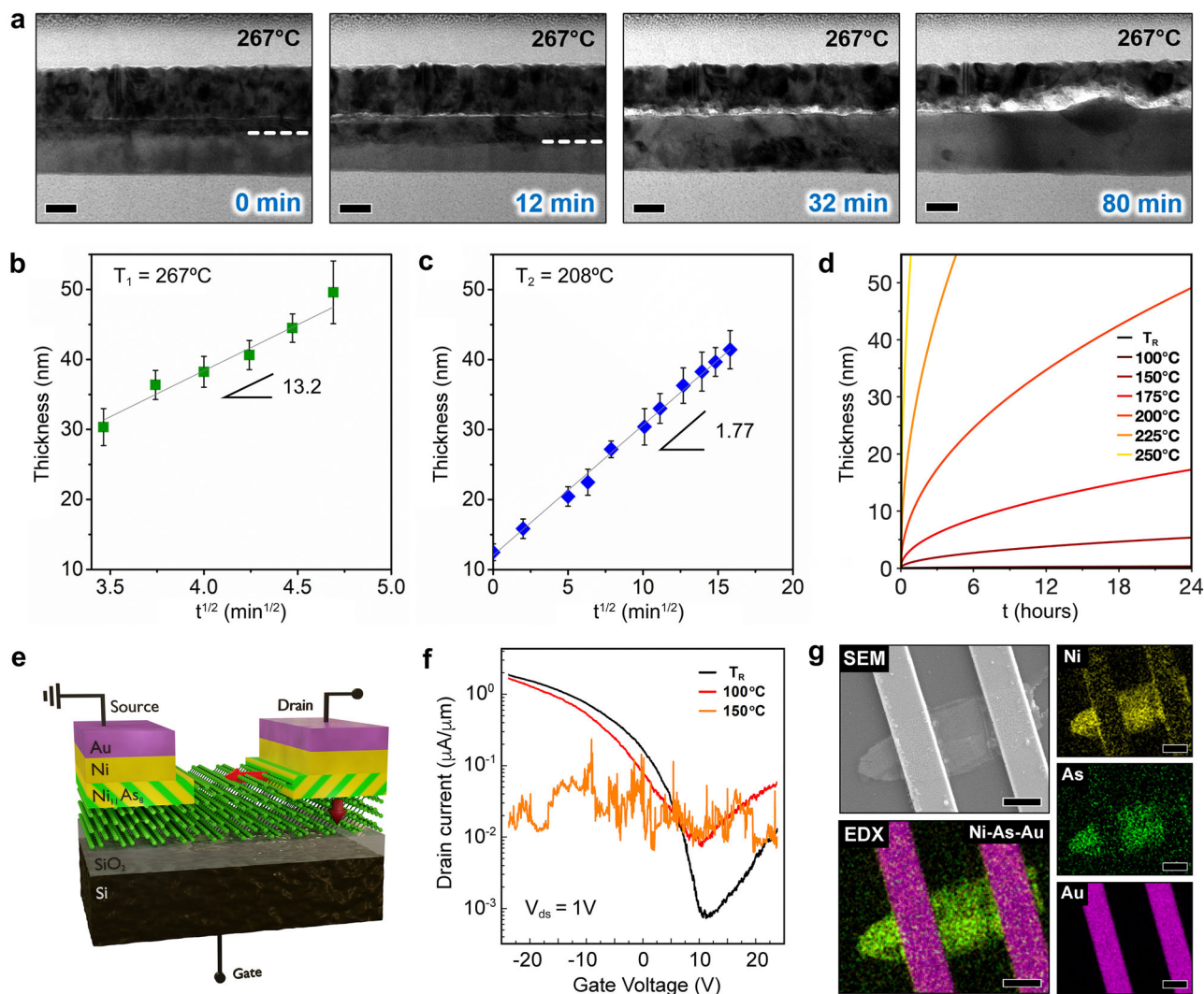


Fig. 3 Diffusion of nickel into b-As and the effects on FET performance. **a** A set of BF-TEM images of the stack of Si/SiO₂ substrate, b-As film, deposited polycrystalline Ni, and the interfacial Ni₁₁As₈ layer showing the expansion of the Ni₁₁As₈ layer with time at temperature $T_1 = 267^\circ\text{C}$. Scale bar is 30 nm. **b, c** The thickness of the Ni₁₁As₈ layer as a function of \sqrt{t} measured when the sample was kept at $267 \pm 1^\circ\text{C}$ and $208 \pm 2^\circ\text{C}$ showing a linear relationship. The slopes of the linear fits are $13.21 \text{ nm min}^{-1/2}$ at 267°C and $1.77 \text{ nm min}^{-1/2}$ at 208°C . The error bars are based on a statistical analysis of layer thicknesses. **d** Calculated thickness of the Ni₁₁As₈ layer as a function of time for different temperatures based on the estimated diffusion coefficient, $D(T)$. **e** Schematic of the as-fabricated b-As channel FET with a global SiO₂/Si back gate. It also depicts the interfacial Ni₁₁As₈ layer and two different paths for charge transfer between Ni₁₁As₈ contact and b-As (red arrows). **f** Charge transfer characteristics: drain current vs gate voltage of 13 nm-thick b-As channel FETs at T_R and at two elevated temperatures: 100 and 150 °C. **g** SEM image with EDX elemental maps of Ni (yellow), b-As (green), and Au (purple) of a b-As channel FET after heating it to 150 °C showing diffusion of Ni into the b-As channel. EDX maps were constructed using As and Ni L, and Au M emissions. Scale bars are 1 μm .

with shorter penetration depth. It should be noted here that when the temperature of the sample reaches about 328°C , b-As start to show signs of sublimation. Small voids can be seen forming along the b-As layers (see Supplementary Fig. 9). Additional in situ heating measurements performed on free-standing b-As flakes confirmed this observation (see Supplementary Fig. 10).

Quantification of the STEM-EDX maps measured from the in situ heated sample after cooling it down to T_R (Fig. 4a), revealed that the compound formed at the interface is about 48 at.% Cr and 52 at.% As. It suggests that the polycrystalline interfacial layer should be orthorhombic CrAs. Similar to Ni₁₁As₈, orthorhombic CrAs also have the highest negative formation energy ($\Delta G_0 = -0.191 \text{ eV}$) among known CrAs compounds³⁰. Additional electron diffraction measurements from the layer stack showed distinct spots corresponding to orthorhombic CrAs further confirming the phase (see

Supplementary Fig. 9). Polycrystallinity of the layer is identifiable in BF-TEM images (see Supplementary Fig. 11).

Next, 50 nm-thick-layer of Ti was deposited onto b-As film. ADF-STEM images and EDX maps obtained at T_R from the interface between Ti and b-As show different kinds of diffusion kinetics (Fig. 4b). Unlike Ni and Cr cases, here As is diffusing into Ti. As can be seen from the high-resolution ADF-STEM image in Fig. 4b, this TiAs_x interfacial layer is only 2-nm-thick. During in situ heating experiments, it was observed that the onset of visible diffusion of As into Ti occurs at 234°C . Further increase of the temperature expedites As diffusion with clear depletion of As from b-As and increases the thickness of the interfacial TiAs_x layer, similar to previous observations with other metals. However, even after reaching $T = 383^\circ\text{C}$ the thickness of the TiAs_x compound layer stayed $< 5 \text{ nm}$. After completion of in situ heating, the sample was cooled to T_R and characterized

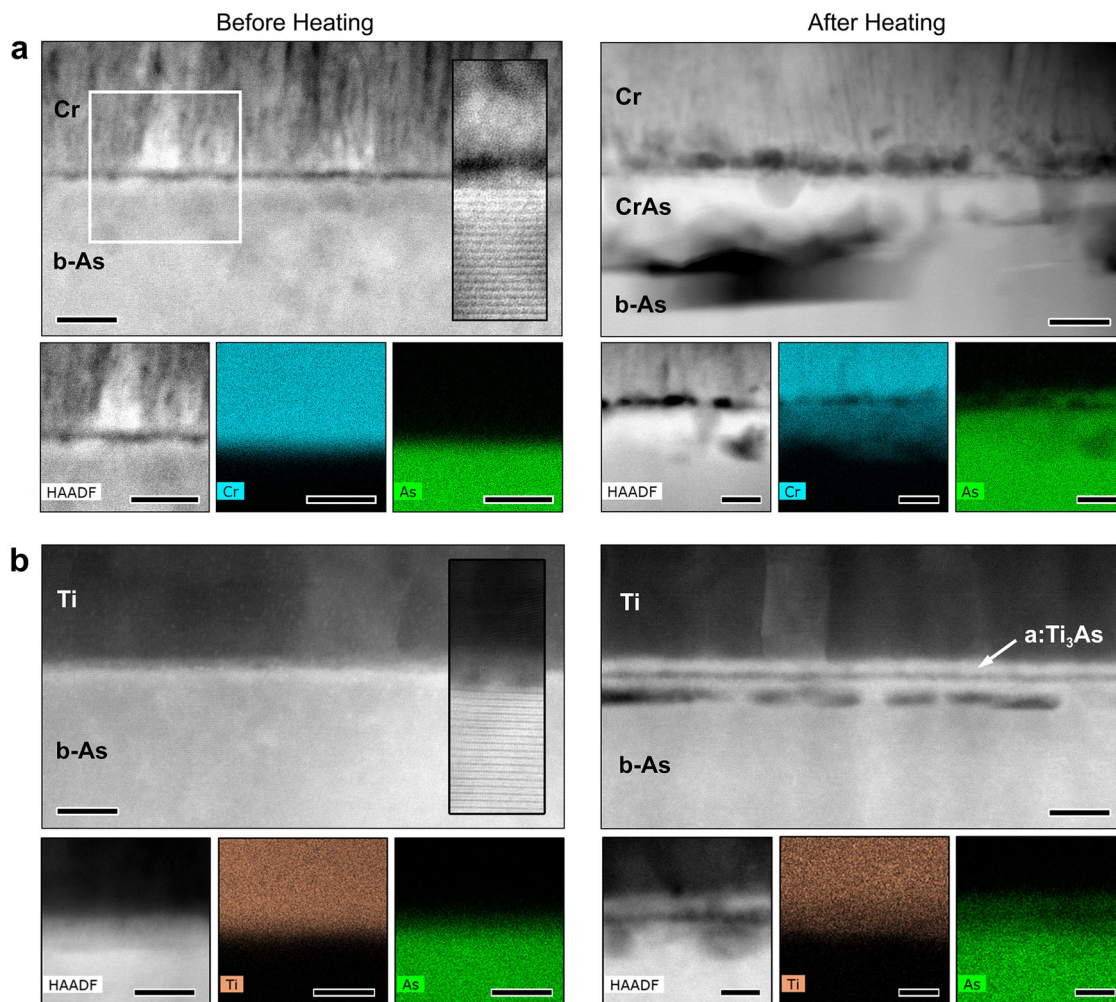


Fig. 4 Formation of the intermetallic layer at the contact with chromium and titanium. **a** ADF-STEM images of the interface of the deposited polycrystalline Cr and b-As film before and after in situ heating. Scale bars are 10 nm. Below are close-up ADF-STEM images of the interface with corresponding EDX elemental maps of Cr (blue), As (green) showing slight diffusion of Cr into b-As before heating and dramatic diffusion and formation of CrAs after heating, reaching 328 °C. Scale bars are 10 nm. **b** ADF-STEM images of the interface of the deposited polycrystalline Ti and b-As film before and after in situ heating. Scale bars are 10 nm. Below are close-up ADF-STEM images of the interface with corresponding EDX elemental maps of Ti (orange), As (green). They show slight diffusion of As into Ti before heating and considerable diffusion and formation of amorphous Ti_3As (a: Ti_3As) after heating reaching 328 °C. The EDX elemental maps are based on As, Cr, and Ti K emissions. Scale bars are 3 nm.

again. BF-TEM images did not show polycrystallinity, as was the case with Ni and Cr, but rather mostly amorphous-like TiAs_x layer (see Supplementary Fig. 12). Figure 4b shows ADF-STEM images and STEM-EDX elemental maps of the interface after cooling to T_R . Quantification of the elemental maps indicates that the layer composition is about 78 at.% Ti and 22 at.% As, which is close to Ti_3As . It should be noted that Ti_3As is not the compound with the highest negative formation energy (that is TiAs)³⁰. While the existence of a new kind of metal contact and its sensitivity to temperature is demonstrated here, additional study is needed to determine the key factors that allow for some of the metals like Ni, Cr, and Ti to form these interfacial layers with b-As and not for others like Pt or Ge (for STEM analysis of deposited Pt and Ge see Supplementary Figs. 13 and 14).

In conclusion, it is observed that when metallic Ni is deposited onto layered b-As using an e-beam evaporator, an interfacial layer of intermetallic $\text{Ni}_{11}\text{As}_8$ is formed dramatically changing the metal contact. In the FETs with b-As as a channel, this new structurally and electronically different interfacial layer also introduces a second and more efficient lateral charge transfer path from metallic contact into the b-As. It is also observed that

deposition temperature and temperature of the contact have a significant effect on the thickness and crystallinity of this interfacial $\text{Ni}_{11}\text{As}_8$ layer. Since Cr and Ti also showed the similar formation of interfacial intermetallic layers, when deposited onto b-As, it is expected that such structurally, compositionally, and electronically different metal contacts with vdW layered materials should exist in other systems and device configurations. The existence of these tunable interfacial layers could provide new pathways for engineering highly efficient metal contacts and device architectures.

Methods

Sample preparation. Layered b-As nanosheets used in this study, were exfoliated from a bulk b-As crystal (bought from 2D Semiconductors Inc.), which was grown by Chemical Vapor Deposition (CVD) using an arsenic precursor. Mechanical exfoliation of b-As from the bulk crystal was carried out using Scotch tape. Subsequently, the flakes were transferred onto a polydimethylsiloxane (PDMS) stamp (Sylgard 184, Dow Corning Co.). The PDMS containing the flakes was stamped onto a SiO_2 (100 nm)/Si wafer (containing Au identification marks), which led to the deposition of b-As flakes on the substrate. To avoid oxidation in air, the substrates were quickly transferred to the e-beam evaporator chamber which was pumped down to a pressure of 10^{-6} Torr. Subsequently, 50/100 nm thick blanket layer of elements like Ni, Cr, Ti, Ge, and Pt were deposited at a rate of 1 \AA s^{-1}

(the rate was 0.6 \AA s^{-1} for Pt) onto the substrate containing the b-As flakes using commercial evaporator (Model SEC600RAP PLC from CHA Industries, Inc.). The chamber/substrate temperature was continuously monitored to ensure that it does not rise above $50 \text{ }^\circ\text{C}$ (besides Pt). To have a uniform coating of the metal film, a rotating (30 rpm) lift-off fixture was used, during the deposition process. The typical time for metal deposition was about 10 min.

A 40 nm layer of amorphous C was sputtered using an SEM sputter coater. A focused Ion Beam instrument (FEI Helios NanoLab G4 dual-beam focused ion beam) was used to make thin, electron transparent lamella. The prepared specimen was adhered onto Cu half grids by Pt deposition using GIS (Gas Injection System) attached to the FIB. To protect the top layer from high-energy ion beam during the FIB sectioning of the lamella, 1–2 μm layer of Pt was deposited before making the trenches. An ion beam with an accelerating voltage of 30 kV was used to make a thin lamella. In the later stages of thinning, an ion beam with an accelerating voltage of 2 kV was used to remove the damaged surface layer. An electron beam of 10 keV was used throughout, to monitor the thinning of the lamella using an ion beam.

In situ TEM experiments. The heating experiments were performed using Gatan double-tilt heating holder on FEI Tecnai G2 F30 Field-Emission Gun (operated at 300 kV) or FEI Tecnai T12 Thermionic Gun (operated at 120 kV) TEM. Imaging was performed in conventional TEM mode. Two types of heating experiments were designed to study the diffusion of elements into b-As. In the increasing temperature mode, the sample was heated to a specified temperature for 15–30 min till images and diffraction patterns were acquired and then increased to a higher temperature. Thus, the temperature was increased in steps to monitor the dynamics of phase transformation. In isothermal heating mode, the temperature is quickly increased to the desired temperature and then maintained at that temperature to monitor the transformation as a function of time.

Ex-situ STEM experiments. ADF-STEM and conventional TEM imaging was performed on an aberration-corrected FEI Titan G2 60-300 STEM equipped with CEOS DCOR probe corrector and super-X energy-dispersive X-ray spectrometer. Imaging and diffraction were carried out at an accelerating voltage of 200 kV. ADF-STEM imaging was done at a camera length of 130 mm and convergence angle of 18.2 or 25.5 mrad with the detector inner and outer collection angles of 55 and 200 mrad respectively. Beam current ranging from 30 to 500 pA was used to perform imaging and EDX spectra acquisitions. Additional ADF-STEM imaging and STEM-EDX maps were obtained using Thermo Fisher Talos F200X G2 STEM equipped with Super-X EDX spectrometer operated at 200 kV and with a probe convergence angle of 10.5 mrad. STEM-EDX maps were acquired at a beam current of 305 pA.

ADF-STEM image simulations. ADF-STEM images of maucherite $\text{Ni}_{11}\text{As}_8$ were simulated using the *Multislice* method and TEMSIM code developed by Kirkland^{34,35}. The maucherite $\text{Ni}_{11}\text{As}_8$ has a tetragonal unit cell with space group $P4_12_12$ and lattice parameters: $a = b = 6.872 \text{ \AA}$, and $c = 21.821 \text{ \AA}$ ²⁸. ADF-STEM images of two orientations of $\text{Ni}_{11}\text{As}_8$ crystal were simulated: [100] and [031]. The specimen thicknesses of $\text{Ni}_{11}\text{As}_8$ for [100] from 12.4 to 41.3 nm for [100] projection and 12.0 to 48.1 nm for [031] were used, which covers a wide range of sample thicknesses for the wedge-shaped prepared samples. The supercell sizes were $21.85 \times 20.68 \text{ \AA}^2$ and $82.72 \times 95.14 \text{ \AA}^2$, for [100] and [031] projections, respectively. A grid size of 1024×1024 pixels was used. For these simulated images, the STEM probes were scanned with 37 pixels/ \AA , 12 pixels/ \AA steps for [100] and [031] projections, respectively. The slice thickness was chosen to be 1 \AA . The following STEM parameters were used to simulate the images: $E_0 = 200 \text{ keV}$, $C_{s(3)} = 0$, $C_{s(5)} = 0$, $\Delta f = 0$, $\alpha_{\text{obj}} = 25 \text{ mrad}$. Electrons within an angle of 50 to 200 mrad were collected to form the ADF-STEM images. Thermal vibrations of the atoms were modeled by averaging ten different frozen phonon configurations for each image. The following room temperature ($T = 300 \text{ K}$) RMS atomic displacements for Ni and As were used: 0.067 \AA and 0.074 \AA respectively²⁸. The final simulated images were convoluted with 2D Gaussian function with the full width at half maximum (FWHM) of 1 \AA to incorporate effects of the source size³⁶.

SEM measurements. SEM images and EDX maps of FETs were obtained using JEOL 6500 Field-Emission Gun SEM equipped with Aztec EDX analytical system from Oxford Instruments. The SEM was operated at 5 kV.

Data availability

The main data supporting the findings of this study are available within this article and its Supplementary Information. Further data are available from the corresponding authors upon request.

Received: 25 July 2021; Accepted: 19 January 2022;

Published online: 17 February 2022

References

- Geim, A. K. & Novoselov, K. S. The rise of graphene. *Nat. Mater.* **6**, 183–191 (2007).
- Eda, G. et al. Photoluminescence from chemically exfoliated MoS_2 . *Nano Lett.* **11**, 5111–5116 (2011).
- Nicolosi, V., Chhowalla, M., Kanatzidis, M. G., Strano, M. S. & Coleman, J. N. Liquid exfoliation of layered materials. *Science* **340**, 1226419 (2013).
- Voiry, D. et al. Enhanced catalytic activity in strained chemically exfoliated WS_2 nanosheets for hydrogen evolution. *Nat. Mater.* **12**, 850–855 (2013).
- Liu, H. et al. Phosphorene: an unexplored 2D semiconductor with a high hole mobility. *ACS Nano* **8**, 4033–4041 (2014).
- Castellanos-Gomez, A. et al. Isolation and characterization of few-layer black phosphorus. *2D Mater.* **1**, 25001 (2014).
- Manzeli, S., Ovchinnikov, D., Pasquier, D., Yazyev, O. V. & Kis, A. 2D transition metal dichalcogenides. *Nat. Rev. Mater.* **2**, 1–15 (2017).
- Illarionov, Y. Y. et al. Insulators for 2D nanoelectronics: the gap to bridge. *Nat. Commun.* **11**, 1–15 (2020).
- Rycerz, A., Tworzyno, J. & Beenakker, C. W. J. Valley filter and valley valve in graphene. *Nat. Phys.* **3**, 172–175 (2007).
- Radisavljevic, B., Radenovic, A., Brivio, J., Giacometti, V. & Kis, A. Single-layer MoS_2 transistors. *Nat. Nanotechnol.* **6**, 147–150 (2011).
- Li, L. et al. Black phosphorus field-effect transistors. *Nat. Nanotechnol.* **9**, 372 (2014).
- Han, W., Kawakami, R. K., Gmitra, M. & Fabian, J. Graphene spintronics. *Nat. Nanotechnol.* **9**, 794–807 (2014).
- Chhowalla, M., Jena, D. & Zhang, H. Two-dimensional semiconductors for transistors. *Nat. Rev. Mater.* **1**, 1–15 (2016).
- Chen, Y. et al. Black arsenic: a layered semiconductor with extreme in-plane anisotropy. *Adv. Mater.* **30**, 1800754 (2018).
- Kandemir, A., Iyikanat, F. & Sahin, H. Monitoring the crystal orientation of black-arsenic via vibrational spectra. *J. Mater. Chem. C* **7**, 1228–1236 (2019).
- Zhong, M. et al. Thickness-dependent carrier transport characteristics of a new 2D elemental semiconductor: black arsenic. *Adv. Funct. Mater.* **28**, 1802581 (2018).
- Golani, P. et al. Ambipolar transport in van der Waals black arsenic field effect transistors. *Nanotechnology* **31**, 405203 (2020).
- Walia, S. et al. Characterization of metal contacts for two-dimensional MoS_2 nanoflakes. *Appl. Phys. Lett.* **103**, 232105 (2013).
- Kappera, R. et al. Phase-engineered low-resistance contacts for ultrathin MoS_2 transistors. *Nat. Mater.* **13**, 1128–1134 (2014).
- Jena, D., Banerjee, K. & Xing, G. H. Intimate contacts. *Nat. Mater.* **13**, 1076–1078 (2014).
- Allain, A., Kang, J., Banerjee, K. & Kis, A. Electrical contacts to two-dimensional semiconductors. *Nat. Mater.* **14**, 1195–1205 (2015).
- Kim, C. et al. Fermi level pinning at electrical metal contacts of monolayer molybdenum dichalcogenides. *ACS Nano* **11**, 1588–1596 (2017).
- Liu, Y. et al. Approaching the Schottky–Mott limit in van der Waals metal–semiconductor junctions. *Nature* **557**, 696–700 (2018).
- Wang, Y. et al. Van der Waals contacts between three-dimensional metals and two-dimensional semiconductors. *Nature* **568**, 70–74 (2019).
- Wu, R. J. et al. Visualizing the metal– MoS_2 contacts in two-dimensional field-effect transistors with atomic resolution. *Phys. Rev. Mater.* **3**, 111001 (2019).
- Smyth, C. M., Addou, R., McDonnell, S., Hinkle, C. L. & Wallace, R. M. Contact metal– MoS_2 interfacial reactions and potential implications on MoS_2 -based device performance. *J. Phys. Chem. C* **120**, 14719–14729 (2016).
- Yun, H., Ghosh, S., Golani, P., Koester, S. J. & Mkhoyan, K. A. Layer dependence of dielectric response and water-enhanced ambient degradation of highly anisotropic black As. *ACS Nano* **14**, 5988–5997 (2020).
- Fleet, M. E. The crystal structure of maucherite ($\text{Ni}_{11}\text{As}_8$). *Am. Mineral. J. Earth Planet. Mater.* **58**, 203–210 (1973).
- Singleton, M. & Nash, P. The As–Ni (Arsenic–Nickel) system. *J. Phase Equilibria* **8**, 419 (1987).
- Jain, A. et al. Commentary: the materials project: a materials genome approach to accelerating materials innovation. *Apl. Mater.* **1**, 11002 (2013).
- Naoi, D. & Kajihara, M. Growth behavior of Fe_2Al_5 during reactive diffusion between Fe and Al at solid-state temperatures. *Mater. Sci. Eng. A* **459**, 375–382 (2007).
- Bourne, H. C. Jr, Chow, L. G. & Bartran, D. S. Deposition temperature of evaporated permalloy films. *J. Vac. Sci. Technol.* **8**, 619–621 (1971).
- Wang, L. et al. One-dimensional electrical contact to a two-dimensional material. *Science* **342**, 614–617 (2013).
- Cowley, J. M. & Moodie, A. F. The scattering of electrons by atoms and crystals. I. A new theoretical approach. *Acta Crystallogr.* **10**, 609–619 (1957).
- Kirkland, E. J. *Advanced Computing in Electron Microscopy* (Springer, 1998).
- Jeong, J. S., Odlyzko, M. L., Xu, P., Jalan, B. & Mkhoyan, K. A. Probing core-electron orbitals by scanning transmission electron microscopy and measuring the delocalization of core-level excitations. *Phys. Rev. B* **93**, 165140 (2016).

Acknowledgements

This project was partially supported by the University of Minnesota (UMN) MRSEC program DMR-1420013 and DMR-2011401 and SMART, one of seven centers of nCORE, a Semiconductor Research Corporation program, sponsored by NIST. This work was partially supported by NPRP Grant no. NPRP10-0206-170366 from the Qatar National Research Fund (a member of the Qatar Foundation). Parts of this work was carried out in the College of Science and Engineering Characterization Facility, the University of Minnesota, supported in part by the NSF through the UMN MRSEC. P.G. and S.J.K. were supported by the NSF under Award No. ECCS-1708769. Portions of this work were conducted in the Minnesota Nano Center, which is supported by the NSF through the National Nanotechnology Coordinated Infrastructure (NNCI) under Award Number ECCS-2025124. The authors also would like to thank Glenn Kuschke and Supriya Ghosh for their insightful discussions.

Author contributions

S.K., K.A.M., and S.J.K. conceived and designed the project. S.K. carried out all TEM and STEM sample preparation, experiments, and data analysis. P.G. deposited flakes, metal films, and carried out all device measurements with input and supervision from S.J.K. H.Y. carried out all SEM sample preparation, experiments, and data analysis. S.G. performed STEM measurements and analysis of individual grains. S.K. and S.G. performed image simulations. K.M.Y. helped with diffusion data analysis and interpretation. S.K. and K.A.M. prepared the manuscript with contributions from all authors.

Competing interests

The authors declare no competing interests.

Additional information

Supplementary information The online version contains supplementary material available at <https://doi.org/10.1038/s43246-022-00233-7>.

Correspondence and requests for materials should be addressed to K. Andre Mkhoyan.

Peer review information *Communications Materials* thanks Iddo Amit and Na Ni for their contribution to the peer review of this work. Primary Handling Editors: Cecilia Mattevi and Aldo Isidori.

Reprints and permission information is available at <http://www.nature.com/reprints>

Publisher's note Springer Nature remains neutral with regard to jurisdictional claims in published maps and institutional affiliations.



Open Access This article is licensed under a Creative Commons Attribution 4.0 International License, which permits use, sharing, adaptation, distribution and reproduction in any medium or format, as long as you give appropriate credit to the original author(s) and the source, provide a link to the Creative Commons license, and indicate if changes were made. The images or other third party material in this article are included in the article's Creative Commons license, unless indicated otherwise in a credit line to the material. If material is not included in the article's Creative Commons license and your intended use is not permitted by statutory regulation or exceeds the permitted use, you will need to obtain permission directly from the copyright holder. To view a copy of this license, visit <http://creativecommons.org/licenses/by/4.0/>.

© The Author(s) 2022